The role of exciton lifetime for charge generation in organic solar cells at negligible energy level offsets

Andrej Classen,[1] Christos L. Chochos,[2,3] Larry Lüer,*[1] Vasilis G. Gregoriou,[2,4] Jonas Wortmann,[1] Andres Osvet,[1] Karen Forberich,[1] Iain McCulloch,[5,6] Thomas Heumueller,*[1] and Christoph J. Brabec*[1,7,8]

[1] *Institute of Materials for Electronics and Energy Technology (i-MEET), Friedrich-Alexander University Erlangen-Nürnberg, Martensstraße 7, 91058 Erlangen, Germany.*

[2] *Advent Technologies SA, Stadiou Street, Platani, Rio, Patras 26504, Greece.*

[3] *Institute of Chemical Biology, National Hellenic Research Foundation (NHRF), 48 Vassileos Constantinou Avenue, 11635 Athens, Greece.*

[4] *National Hellenic Research Foundation (NHRF), 48 Vassileos Constantinou Avenue, 11635 Athens, Greece.*

[5] *Department of Chemistry and Centre for Plastic Electronics, Imperial College London, London SW7 2AZ, UK.*

[6] *King Abdullah University of Science and Technology (KAUST), KAUST Solar Center (KSC), Thuwal 23955-6900, Saudi Arabia.*

[7] *Helmholtz-Institute Erlangen-Nürnberg (HI ERN), Immerwahrstraße 2, 91058 Erlangen, Germany.*

[8] *Bavarian Center for Applied Energy Research (ZAE Bayern), Immerwahrstraße 2, 91058 Erlangen, Germany.*

E-mail: thomas.heumueller@fau.de, larry.lueer@fau.de, christoph.brabec@fau.de

Organic solar cells (OSC) utilize an energy level offset (E_{offset}) to generate free charge carriers. While a very small E_{offset} increases the open-circuit voltage, it remains unclear how exactly charge generation is affected. Here we investigate OSC blends with highest occupied molecular orbital energy level offsets (ΔE_{HOMO}) between donor and acceptor ranging from 0 to 300 meV. We demonstrate that exciton quenching at negligible ΔE_{HOMO} takes place on timescales approaching the exciton lifetime of the pristine materials, drastically limiting external quantum efficiency. We quantitatively describe this finding via the Boltzmann stationary-state equilibrium between charge transfer states and excitons and further reveal a long exciton lifetime to be decisive in maintaining efficient charge generation at negligible

ΔE_{HOMO}. Moreover, the Boltzmann equilibrium quantitatively describes the major reduction in non-radiative voltage losses at very small ΔE_{HOMO}. Ultimately, highly luminescent NIR emitters with very long exciton lifetimes are suggested to enable highly efficient OSCs.

With the emergence of non-fullerene acceptors (NFAs), organic solar cells (OSC) reached power conversion efficiencies (PCE) over 16 %[1,2]. Despite this stark increase in PCE, the open-circuit voltage (V_{OC}) still lag behind inorganic solar cells showing that V_{OC} losses are still substantial[3–6]. An important aspect related to V_{OC} losses is the energy level offset (E_{offset}) at the donor-acceptor interface which provides the driving force for splitting excitons into free charge carriers[7]. To avoid excessive voltage losses, the offset should be as small as possible. At the same time, though, it is generally believed that an energy level offset of at least 0.3 eV is necessary to obtain fast and efficient charge separation[7]. Nevertheless, it has been recently shown that by fine-tuning the energy levels in high-performance NFAs to an E_{offset} smaller than 0.2 eV, the band gap to V_{OC} losses could be lowered from more than 0.8 V to around 0.6 V in highly efficient OSCs[1,2,8,9]. However, it remains unclear how efficient charge generation can be maintained at such small driving forces for exciton splitting. For instance, very slow charge generation on the order of 20 ps were reported in OSCs based on low E_{offset} systems.[10] Charge generation in these systems is slow compared to femtosecond charge generation in conventional OSCs where a large energy offset afford a strong driving force. This observation thus raises the question of how charge generation in OSCs is affected at negligible energy level offsets and how this limits performance of OSCs.

In this work, we address this question by investigating a representative number of OSC blends with offsets between the donor and acceptor highest occupied molecular orbital energies

(ΔE_{HOMO}) spanning from 0 to 300 meV. At negligible ΔE_{HOMO} we detect ultra-slow exciton splitting with lifetimes up to 1300 ps, which reaches or even exceeds the pristine materials´ exciton lifetimes. This drastically limits charge generation and we demonstrate a strong correlation between the exciton splitting efficiency and the external quantum efficiency (EQE). Based on these experimental findings, we postulate a very long exciton lifetime as the key parameter to maintain efficient device operation at negligible ΔE_{HOMO}. The importance of this design criteria is verified by an analytic model based on the Boltzmann stationary-state equilibrium between local exciton (LE) and charge transfer (CT) state, which quantitatively describes the quantum efficiency for charge generation as a function of two parameters only: energy offsets and singlet exciton lifetime. Moreover, this effective "two states" model provides striking insights into the experimentally observed steep drop of non-radiative voltage losses ($\Delta V_{OC,non\text{-}rad}$) approaching zero ΔE_{HOMO}, as this can be quantitatively explained by a shift of the Boltzmann equilibrium from CT states towards exciton states. In particular, the steep drop occurs at a maximum slope of 0.8 V/eV, which we show to be the expected value if the drop is caused by a Boltzmann equilibrium between two states whose ratio of emissive quantum yields is 0.01.

Donor:acceptor systems with different energy offsets

To analyze the limitations in device operation of OSCs at very small E_{offset}, we investigated each combination of four high performance NFAs with a series of four newly synthesized donor-acceptor (D-A) type conjugated polymers consisting of benzodithiophene and quinoxaline derivatives, see Figure 1a. By using fluorine or sulfur atom functionalization or a combination, we can control E_{HOMO} of the donor polymers in increments of roughly 0.06 eV, allowing for a fine tuning of ΔE_{HOMO} when matching the energy levels of polymer donor and small molecule

acceptor. The relative changes in polymer E_{HOMO} based on DFT calculations are reported in Supplementary Figure 1.

The donor polymers are denoted according to our notation as WF3, WF3S, WF3F and WF3FS. In particular, WF3F (also known as PBQ-4F[9]) and WF3FS exhibit deep polymer E_{HOMO}. To obtain well-matched energy levels, we chose four high performance NFAs which were reported to exhibit relatively shallow acceptor E_{HOMO} of -5.5 eV to -5.6 eV[2,10–12]. The NFAs are commonly used high-performance acceptors, namely 3,9-bis(2-methylene-(3-(1,1-dicyanomethylene)-indanone))-5,5,11,11-tetrakis(4-hexylphenyl)-dithieno[2,3-d:2',3'-d']-s-indaceno[1,2-b:5,6-b']dithiophene (ITIC)[13], two different rhodanine flanked small molecules (o-IDTBR and eh-IDTBR)[12] and the recently reported acceptor Y6[14]. In addition, we also investigated a large E_{offset} system as a reference, based on the fullerene acceptor [6,6]-Phenyl-C71-butyric acid methyl ester ($PC_{70}BM$), which exhibits a deep E_{HOMO} of -5.96 eV.

A full overview of the energy level alignment is shown in Figure 1b, based on previously reported energy levels determined by cyclic voltammetry (CV) in solution[2,9,10,12–15]. However, energy levels of pristine donor and acceptor materials can differ in a donor:acceptor blend with respect to the pristine material's energy levels[16,17]. For ITIC we observed a reduced E_{HOMO} upon blending with WF3 by CV on blend films, see Supplementary Figure 2, and thus added our measured value in Figure 1b. For the other acceptors we do not observe significant changes in E_{HOMO}, see Supplementary Figure 2. We note that generally CV cannot be used as a reliable method to determine precise E_{HOMO} levels and thus also exact driving forces for charge generation[18]. On the other hand, electroluminescence quantum efficiency or non-radiative voltage losses serve as a significantly better benchmark for evaluating energy level offsets[18]. Nevertheless, in several systems E_{HOMO} is expected to almost match perfectly, which results in very small driving forces for hole transfer. We note, that due to the larger band gap of the

polymers, the offset in E_{LUMO} is not a limiting factor. As a general note we mention that unless explicitly mentioned in an individual case, the driving force for charge generation refers to ΔE_{HOMO}.

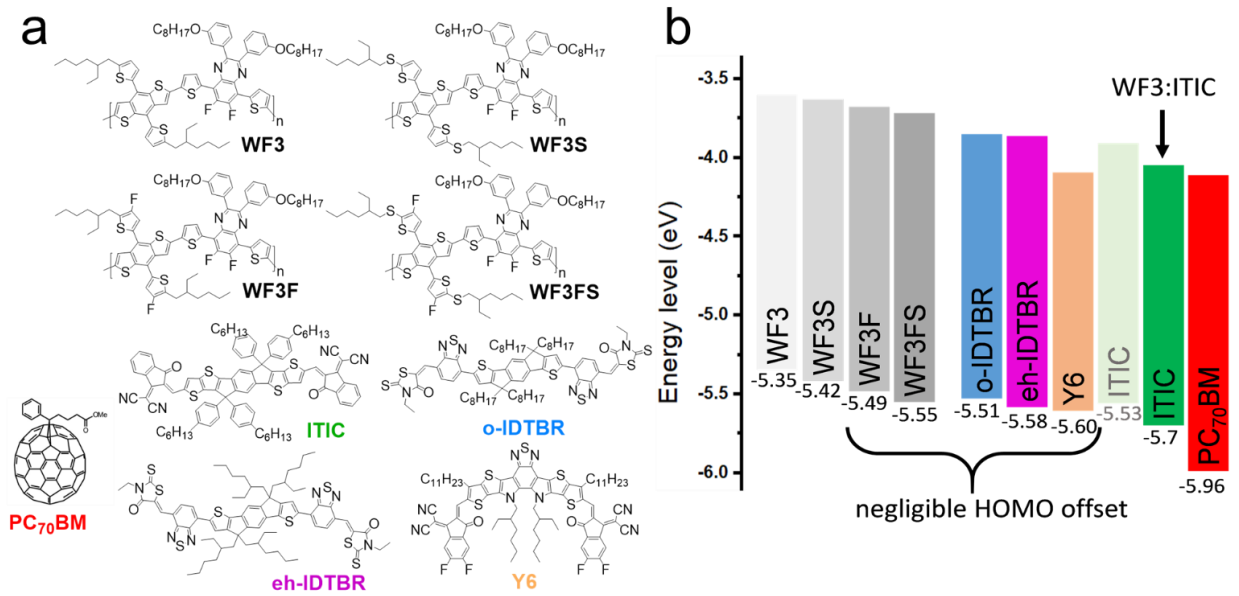

Figure 1 | Donor and acceptor materials and their energy level alignment. a) Chemical structure of the donor polymers (WF3, WF3S, WF3F and WF3FS, indicated in grey) and small-molecule acceptors ($PC_{70}BM$, ITIC, eh-IDTBR, o-IDTBR, Y6, indicated in colour) investigated in this study. **b)** Energy level diagram determined by cyclic voltammetry in solution, and reported in literature[2,9,11,12]. A shift of energy levels may occur in donor:acceptor blends[16,17] as observed for WF3:ITIC, see Supplementary Figure 2. For some combinations of these donors and acceptors, negligible offsets in E_{HOMO} are expected, which results in very small driving forces for exciton splitting.

Exciton splitting efficiencies

A viable method to investigate the exciton splitting lifetime is to measure the quenching of photoluminescence (PL), by time-resolved photoluminescence (TRPL) measurements. The experimentally observed rate of exciton decay in bulk heterojunction (BHJ) solar cells is the sum of intrinsic (radiative and non-radiative) decay and exciton dissociation at the interface. To determine the exciton splitting lifetime in a BHJ it is thus necessary to account for the lifetime of the singlet exciton.

As a first step we therefore measured TRPL of all pristine donor and acceptor materials on non-annealed layers on glass, see Figures 2a and 2b, which we observed to be representative for the exciton dynamics of the acceptor materials in BHJ solar cells, see Supplementary Figure 3. However, as outlined in Supplementary Note 1 and in Supplementary Figure 4a, the singlet exciton lifetime of all donors used in this work is very similar and around 800 ps. For the acceptors used in this work we observe a significant spread in singlet lifetimes (Supplementary Figure 4b). Interestingly, we find that Y6 exhibits the longest exciton lifetime of around 1000 ps.

At the excitation wavelength of 402 nm, we create excitons in both donor and acceptor materials, see ground state absorption spectra in Supplementary Figures 32 - 35 and Supplementary Note 4. However, we observe nearly exclusively the PL spectrum of the lower bandgap component which is the acceptor (see Supplementary Figures 36 and 37). Excitons in the higher bandgap component (donor) have high driving force for dissociation, which is known to result in ultrafast exciton dissociation[19,20]. We have quantified the residual amount of donor emission contributing to the TRPL traces to be typically in the lower percent range, with a maximum of about 13% (see Supplementary Figures 32 - 35). Even at this level of donor PL, a tri-exponential evaluation of TRPL traces should still allow to associate the dominant lifetime to the acceptor exciton.

We now turn to the TRPL analysis of all BHJ devices, see Figures 2c – 2f. TRPL data of all $PC_{70}BM$ based devices are shown in Supplementary Figure 4d. A standard procedure for the extraction of lifetimes was followed, consisting in re-convolution of a fitted tri-exponential curve with the instrumental response function (IRF), allowing to detect lifetimes down to tens of ps. Due to disorder and due to a possible re-generation of excitons after charge recombination[21], PL decay in organic solids is never mono-exponential. However, the fastest decay constants vastly dominate the overall decay in near all our samples. For this reason, we restrict our reasoning on

the fastest rate constants only, which is clearly separate from the slower ones and thus can be obtained with high accuracy. For two examples, WF3 and WF3:ITIC, we show the full re-convolution based fitting in Supplementary Figures 5-10 in Supplementary Note 1. The extracted PL decay lifetimes and exciton lifetimes for all systems are listed in Table 1. Utilizing all PL decay lifetimes and exciton lifetimes we determine the lifetimes of exciton splitting and exciton splitting efficiencies, as outlined in Supplementary Note 1. The exciton splitting lifetimes for both IDTBR derivates exceed 1000 ps which is greater than the respective exciton lifetimes. This drastically diminishes the yield of exciton splitting, see Table 1.

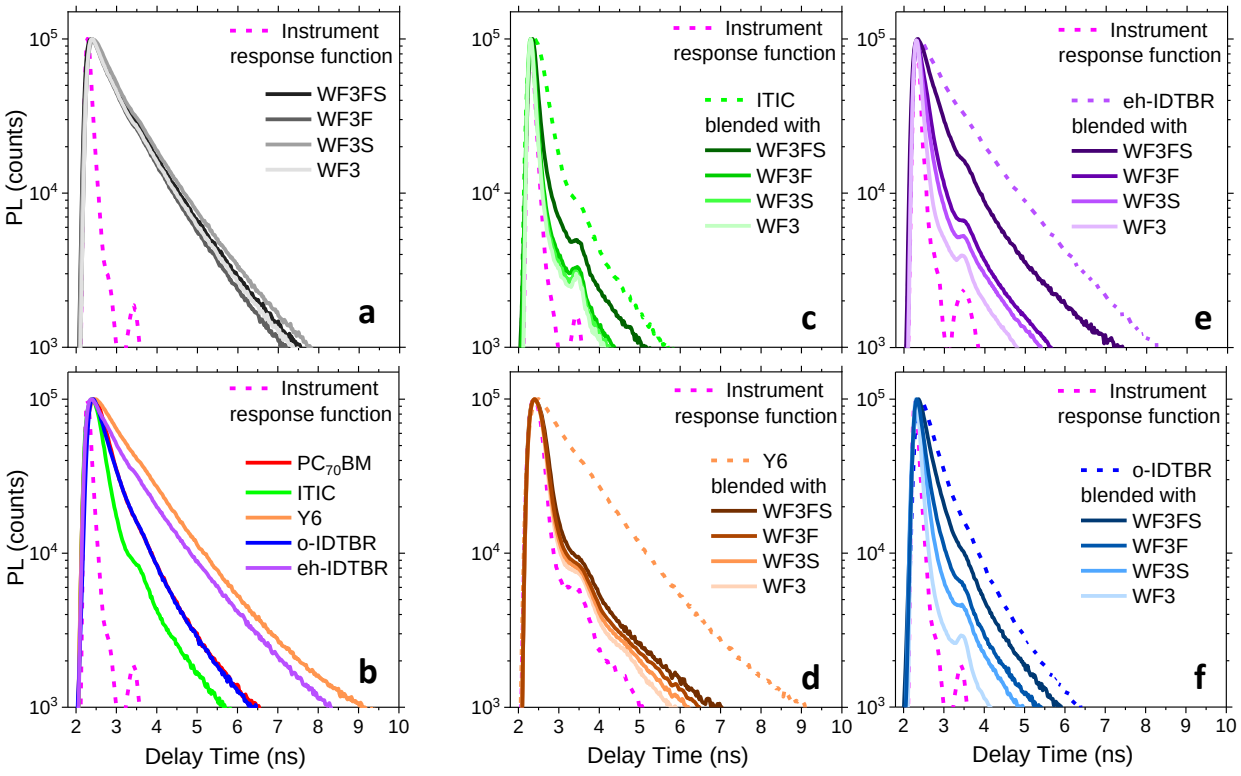

Figure 2 | Exciton dynamics of the donor and acceptor materials and their blends. a), **b)** TRPL of pristine material donors and acceptors (layers on glass) representing the respective singlet exciton lifetime and of **c) – f)** all solar cells investigated in this study, showing the PL quenching in the BHJ. The excitation wavelength is 402 nm for all the sample except for Y6 for which a 783 nm excitation wavelength is used.

Table 1: Fitted values for exciton lifetimes, PL quenching lifetimes and calculated values for exciton splitting lifetimes and exciton splitting efficiencies. The fits and calculations are described in detail in Supplementary Note 1. All lifetimes are given in picoseconds.

	Exciton lifetimes
ITIC	305.3
Y6	1016
eh-IDTBR	898.3
o-IDTBR	561.5

	PL quenching lifetimes	**Exciton splitting lifetimes**	**Efficiency of exciton splitting**
WF3:ITIC	24.7	26.9	**0.919**
WF3S:ITIC	27.4	30.1	**0.910**
WF3F:ITIC	29.7	32.9	**0.903**
WF3FS:ITIC	47.5	56.3	**0.844**
WF3:Y6	29.0	29.9	**0.971**
WF3S:Y6	27.4	28.2	**0.973**
WF3F:Y6	39.1	40.7	**0.962**
WF3FS:Y6	41.2	42.9	**0.959**
WF3:eh-IDTBR	39.9	41.8	**0.956**
WF3S:eh-IDTBR	50.8	53.8	**0.943**
WF3F:eh-IDTBR	174.4	216.4	**0.806**
WF3FS:eh-IDTBR	499.1	1123.1	**0.444**
WF3:o-IDTBR	24.5	25.6	**0.956**
WF3S:o-IDTBR	54.8	60.7	**0.902**
WF3F:o-IDTBR	183.9	273.5	**0.672**
WF3FS:o-IDTBR	398.8	1376.7	**0.290**

The exciton splitting efficiencies should directly translate into an efficiency limit for charge generation. Therefore, we present a comparison of the exciton splitting efficiencies and the maximum EQE of devices, see Figure 3a. The EQE spectra of each OSC are shown in Supplementary Figure 11. In Figure 3a we observe an excellent correlation between the exciton splitting efficiencies determined from TRPL measurements and the maximum EQE of devices. To corroborate the relevance of this findings we further determined the IQE spectra by transfer

matrix modelling and found the same strikingly convincing agreement as for EQE measurements (Supplementary Figure 12). Despite an exciton lifetime of only 300 ps, ITIC can maintain a relatively efficient exciton splitting because of a sufficiently large driving force for charge generation, of course at the expense of larger voltage losses, vide infra. Strikingly different, it is the long exciton lifetime over 1000 ps for Y6 which enables efficient exciton splitting at small energy level offsets and considerably reduced voltage losses.

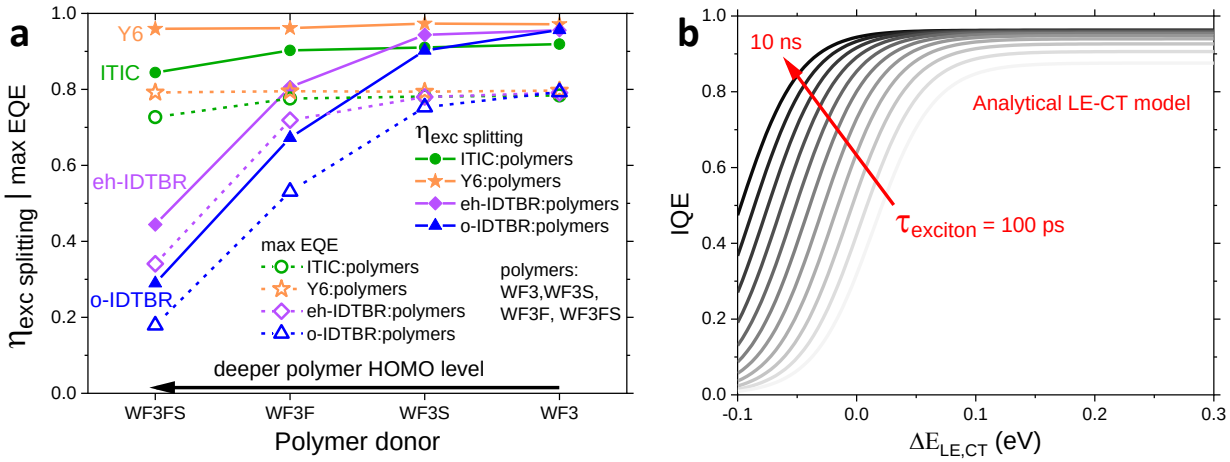

Figure 3 | Exciton splitting efficiency and its correlation with external and internal quantum efficiencies. a) Exciton splitting efficiency derived from TRPL measurements and maximum EQE of devices. The strong correlation shows that inefficient exciton splitting is the main cause of low EQE at very small driving forces for exciton splitting. Solid and dashed lines in between data points serve as guides to the eye. **b)** Calculation of IQE based on an analytical model which incorporates the Boltzmann stationary-state equilibrium between LE and CT states, see Supplementary Note 2. The calculated IQE in dependence of the exciton lifetime reveals that a long exciton lifetime allows to maintain efficient exciton splitting at very small driving forces for exciton splitting.

To understand the ultra-slow quenching of PL for which quenching lifetimes approach the pristine materials' exciton lifetime (as for example for o-IDTBR, see Figure 2f) and the strongly diminished quantum efficiencies (Figure 3a), we developed an effective two-states model to quantitatively describe exciton separation yields as a function of the energy offset and the exciton lifetime (Figure 3b).

The model is based on the solution of the rate equations for excitons (or local exciton – LE) and CT states in Boltzmann stationary-state equilibrium, where charge separated states only can be formed from CT states but not from LE states. This model is justified specifically for small ΔE_{HOMO} as the formation of charge separated states from excitons, typically described by long-range transfer mechanisms[22], requires significant excess energy. The analytic model is described in detail in Supplementary Note 2. Figure 3b shows that the exciton splitting efficiency depends on both the offset in E_{HOMO} and the exciton lifetime. If the exciton lifetime is short, then high exciton splitting efficiencies can only be obtained at significant driving forces. On the other hand, if the exciton lifetime is long, then high splitting efficiencies are possible at negligible ΔE_{HOMO}. Our key conclusion and proposition as design rule for organic solar cells close to the radiative limit is that very long exciton lifetimes are most critical for efficient charge separation in the limit of small driving forces at well-matched energy levels.

Voltage loss analysis

High power-conversion efficiency also requires a high V_{OC} and small offset in E_{HOMO} is considered to be crucial to reduce V_{OC} losses. We therefore investigate the extent to which a small ΔE_{HOMO} is beneficial in achieving a high V_{OC}. We fabricated OSCs with the following device architecture indium tin oxide (ITO)/zinc oxide (ZnO)/active layer/molybdenum oxide (MoO_3)/aluminum (Ag).

The *J-V* characteristics with all V_{OC} values are shown in Figures 4a – 4e, while the parameters of the *J-V* curves are listed in Supplementary Table 3. For all acceptors we observe a clear trend as E_{HOMO} of the polymer is lowered from WF3 to WF3FS, V_{OC} is increased. When the donor and acceptor levels are becoming equal, V_{OC} can no longer be increased. This is observed for WF3FS:o-IDTBR where V_{OC} is almost identical to WF3F:o-IDTBR.

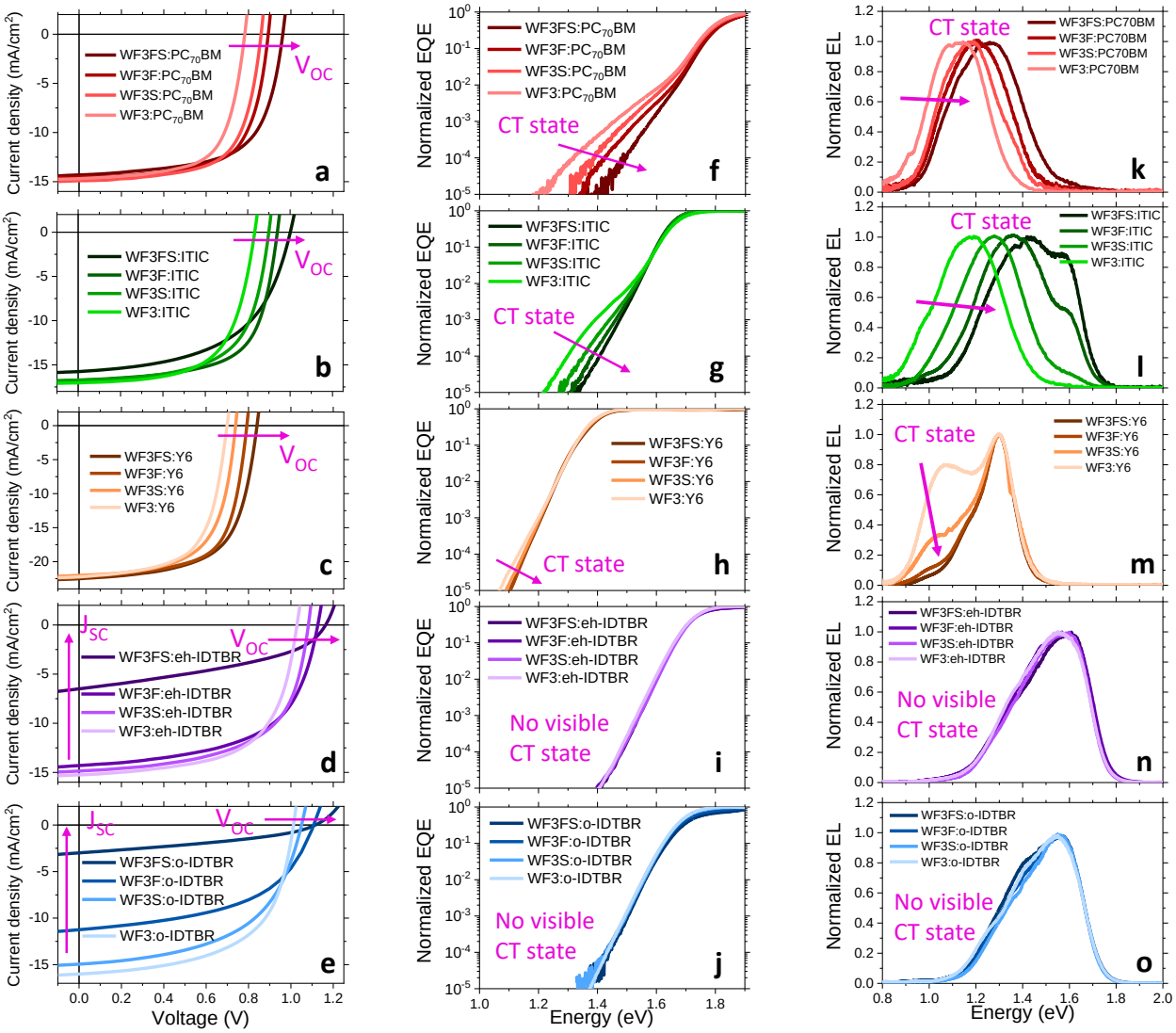

Figure 4 | *JV*-characteristics, FTPS and EL of all solar cells. a) – e) *J-V*-curves of the OSC blends (same devices as in Figure 1). The V_{OC} of all OSCs increases as the HOMO level is consecutively lowered in the series from WF3 to WF3FS. The details of the PV parameters of the device are reported in Supplementary Table 3. **f) – j)** Normalized FTPS-EQE (same devices as JV-curves) and **k) – o)** normalized EL (same devices as JV-curves). FTPS and EL measurements are used to determine the band gap, the band gap to V_{OC} loss and the non-radiative voltage loss for each system. In addition, FTPS and EL reveal clear CT states for systems based on $PC_{70}BM$, ITIC and Y6 while for OSCs based on eh-IDTBR and o-IDTBR no CT state is detected.

While V_{OC} itself is an important value, the respective voltage losses of each system contain the relevant information when comparing different acceptors, as these different acceptors also exhibit different band gaps. A key value is the band gap to V_{OC} loss in a solar cell. In the literature, several procedures have been applied to determine the band gaps of solar cells[23], while to the best of our knowledge only one method is based on a proper mathematical model and also

utilizes the device band gap instead of a material band gap.[24] A precise measurement of the EQE alone is sufficient to determine the band gap and we illustrate the band gap calculation for WF3FS:Y6 in Supplementary Figure 17. We measured EQE accurately over several orders in magnitude by using Fourier-transform photocurrent spectroscopy (FTPS) for all systems (Figures 4f – 4j). Besides allowing for a precise determination of the device band gap, these measurements also reveal the existence of a CT state[25].

Employing detailed balance theory, precise EQE measurements and complementary electroluminescence (EL) measurements are combined (Supplementary Figures 18 – 22) to calculate the radiative V_{OC} ($V_{OC,rad}$)[26,27] in all of our solar cells (see Methods for details). Utilizing the band gap and $V_{OC,rad}$, we determined the total voltage loss and $\Delta V_{OC,non\text{-}rad}$ for all investigated systems, see Figures 5a and 5b. Regarding total voltage losses, composites based on $PC_{70}BM$ exhibit high voltage losses, ITIC-based acceptor composites exhibit moderate losses and the other NFAs have the smallest voltage losses. Especially for WF3FS:o-IDTBR, WF3FS:eh-IDTBR and WF3FS:Y6, we measure exceptionally low voltage losses as small as 0.56 V.

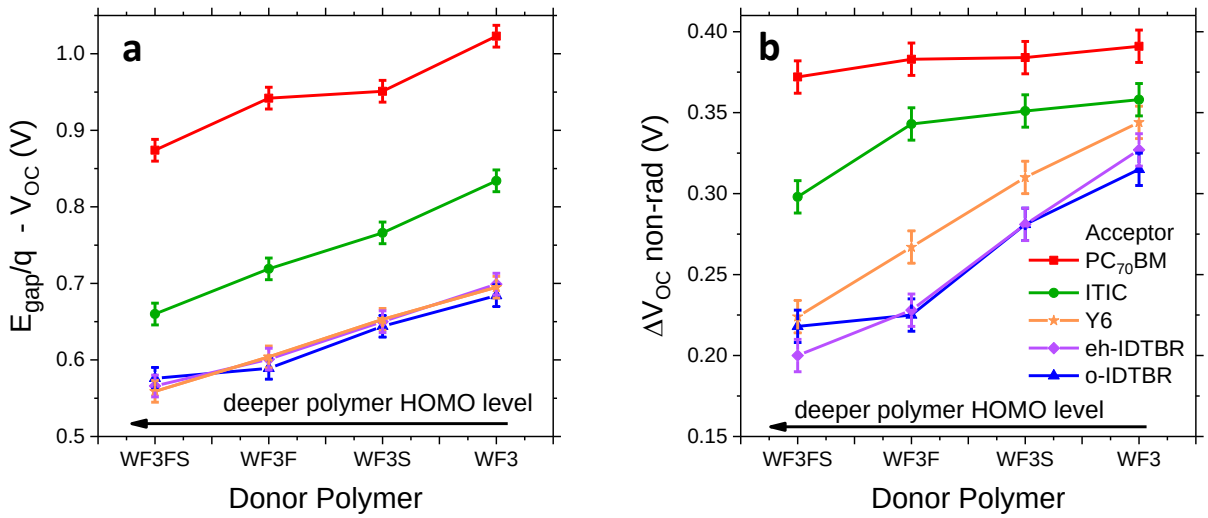

Figure 5 | Voltage loss analysis as a function of the energy level offset. a) Band gap to V_{OC} loss. We observe that WF3FS:Y6 exhibits the lowest total voltage loss. **b)** Non-radiative V_{OC} loss. The $PC_{70}BM$ systems show no significant trend, as the HOMO level is tuned. In contrast, we observe a steep reduction of non-radiative V_{OC} losses for systems with very small offsets in E_{HOMO}. Solid lines in between data points are guides to the eye. The analysis is based on the data presented in Figure 4 (JV-characteristics, FTPS-EQE and EL). The error bars represent an estimation of the upper error limit for the calculation of $V_{OC,rad}$ and for the calculation of the device band gap based on the measurement precision of FTPS-EQE.

Deeper insight is gained by analyzing the non-radiative voltage losses, see Figure 5b. We detect that $PC_{70}BM$ exhibits high non-radiative voltage losses of about 0.4 V. Interestingly we observe no expressed correlation between the HOMO level offset and $\Delta V_{OC,non\text{-}rad}$ for the series from WF3 to WF3FS. In contrast, we notice very clear trends for all NFA based systems and we discover that $\Delta V_{OC,non\text{-}rad}$ is significantly lowered as the HOMO energy levels of polymer and acceptor are becoming better aligned. We further highlight that we find a much better correlation between $\Delta V_{OC,non\text{-}rad}$ and the relative E_{HOMO} offset than between $\Delta V_{OC,non\text{-}rad}$ and the energy of the CT state (E_{CT}). This is a consequence for composites with very low E_{HOMO} offsets which dominantly form hybrid states instead of CT states. In that case, E_{CT} no longer can be determined reliably. On the other hand, for composites with a clearly detected CT states, E_{CT} follows the change in E_{HOMO} (see Figures 4k and 4l for $PC_{70}BM$ and ITIC based devices respectively). Nevertheless, a linear trend for $\Delta V_{OC,non\text{-}rad}$ versus E_{CT} with a slope of roughly -0.2 V/1.0 eV was proposed.[28] When comparing WF3 and WF3FS, E_{HOMO} roughly changes by 0.2 eV and according

to the linear trend, we therefore expect a change of $\Delta V_{OC,non\text{-}rad}$ in the order of -0.04 V. Within the error margins, $PC_{70}BM$ and ITIC are within that range. A significantly different trend is observed for the other three NFAs. For example, Y6 exhibits a total change of -0.12 V from WF3 to WF3FS which corresponds to an average slope of -0.6 V/1.0 eV. Interestingly, a slope of roughly -0.6 V/1.0 eV is also observed for the other devices, which exhibit excellent non-radiative voltage losses. To obtain an improved understanding, we thus plot $\Delta V_{OC,non\text{-}rad}$ versus ΔE_{HOMO} for all systems in Figure 6a. While there is uncertainty in the exact values of ΔE_{HOMO}, as mentioned above, Figure 6a reveals the general trend of steeply reduced $\Delta V_{OC,non\text{-}rad}$ for ΔE_{HOMO} of smaller than 0.2 eV.

Applying the identical effective two-states model introduced before to calculate EQE, we show in Supplementary Note 2 that the steep drop of $\Delta V_{OC,non\text{-}rad}$ for negligible ΔE_{HOMO} is a generic feature of an equilibrium between excitonic and CT states when the density of available excitonic states is significantly larger than the density of CT states.

We have performed a multi-objective optimization, fitting both IQE and $\Delta V_{OC,non\text{-}rad}$ with the same model and the same set of parameters. Varying the radiative and non-radiative decay constants of the CT state (those of the LE state are known) and the extraction rate constant k_{23}, we achieved excellent agreement with the measured dataset for all materials, see Supplementary Figures 28 – 31. In the fits, we have found that the degeneracy ratio g_{12} between LE and CT states is linearly dependent with the CT rate constants; we therefore assumed $g_{12}=0.1$[29]. The most striking finding is that the steep drop of $\Delta V_{OC,non\text{-}rad}$ for vanishing driving forces is rendered quantitatively for all donor/acceptor combinations. In Figure 6b, we have applied an energy shift to all data and fitting functions, such that their inflection points occur at zero energy, and we have normalized the Y axis. In this representation, the curve shape is only weakly depending on the ratio CTQY/LEQY (Supplementary Figure 25f). Thus, for similar values of this ratio a universal

single curve form is obtained that does not depend on the individual CT and LE decay constants. Figure 6b shows that all our data points follow this universal curve shape very closely, which is a strong argument for the presence of a Boltzmann equilibrium governing non-radiative voltage losses at vanishing driving forces for exciton splitting. Finally, for the ratio of 0.01 between CTQY/LEQY (corresponding to 120 mV change in $\Delta V_{OC,non\text{-}rad}$), which is a typical value in the investigated systems, a maximum slope of 0.8 V/eV is expected for $\Delta V_{OC,non\text{-}rad}$. As shown in Supplementary Figure 31, this maximum slope is fully in line with the experimental data.

The fact that even the details of the equilibrium model are rendered by experiment, shows that the Boltzmann equilibrium LE ⇔ CT largely dominates the evolution of $\Delta V_{OC,non\text{-}rad}$ at vanishing driving forces while other factors, such as diffusion limited exciton splitting (microstructure control), slow Marcus rates (Supplementary Note 4), and triplet induced loss paths, do not play a significant role. Finally, this indicates that hybridization, while undoubtedly being present, is per se not the origin of reduced $\Delta V_{OC,non\text{-}rad}$ at small energy level offsets.

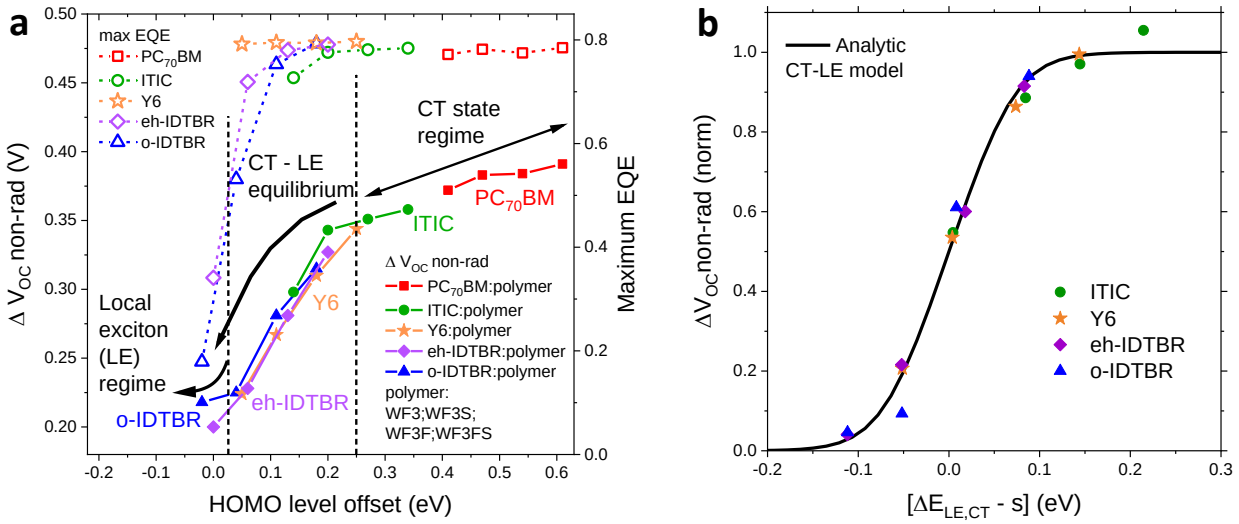

Figure 6 | Experimental and analytic analysis of $\Delta V_{OC,non\text{-}rad}$. a) $\Delta V_{OC,non\text{-}rad}$ and maximum EQE of all solar cells with respect to ΔE_{HOMO} (as significant E_{HOMO} shifts occur upon blending of acceptor with polymer, acceptor E_{HOMO} of ITIC, eh-IDTBR and o-IDTBR is adjusted for the comparison of $\Delta V_{OC,non\text{-}rad}$ between all systems, see Supplementary Figure 23 for details). This inter-system comparison of the maximum EQE at equal $\Delta V_{OC,non\text{-}rad}$ shows that Y6 can maintain an excellent EQE despite the minimal $\Delta V_{OC,non\text{-}rad}$. Further, it reveals the trend of a strongly decreasing $\Delta V_{OC,non\text{-}rad}$ when the energy level offset is tuned to small values. The colored lines in between data points are guides to the eye. The black arrows indicate the respective regimes in which $\Delta V_{OC,non\text{-}rad}$ is solely determined by the CT state properties, solely by the LE state and the intermediate regime in which the CT-LE equilibrium determines $\Delta V_{OC,non\text{-}rad}$. **b)** Universal dependence of the normalized nonradiative voltage loss on the effective energy offset $\Delta E_{LE,CT}$ - s, where s is the inflection point of the corresponding fitted function in Supplementary Figure 28. All data follow the universal curve, thus showing that $\Delta V_{OC,non\text{-}rad}$ at small driving forces are essentially controlled by the Boltzmann stationary-state equilibrium between LE and CT.

Conclusion

We investigated device operation of OSCs at extremely small HOMO level offsets. Utilizing time-resolved PL, we detect ultra-long exciton splitting lifetimes which in some cases even exceed the pristine materials' exciton lifetimes and thereby severely reduce EQE. We further present an analytic effective two-state equilibrium model which describes the experimental findings. The experimental analysis of V_{OC} losses and the analytical model demonstrate that negligible energy level offsets are the key requirement for achieving highly efficient OSCs by reducing $\Delta V_{OC,non\text{-}rad}$. The reduction of $\Delta V_{OC,non\text{-}rad}$ is due to a shift of the CT-LE equilibrium towards LE states of the acceptor material. This causes dominant recombination of excited states

via the LE states instead of CT states. The higher emission yield of LE states thus yields the smaller $\Delta V_{OC,non\text{-}rad}$. However, efficient device operation at negligible offsets can only be maintained if exciton splitting remains efficient. This requires very long exciton lifetimes. Moreover, as long as the radiative decay rate of excitons does not change, a long singlet exciton lifetime is equivalent to a high electroluminescence quantum efficiency enabling improved $\Delta V_{OC,non\text{-}rad}$. As a direct consequence, we suggest that the quest for more efficient organic solar cell materials should be directed to develop highly efficient IR emitters. We further believe that the design rule to look for long exciton lifetime absorbers is of outmost importance for synthetic and especially theoretical chemists, as it can be directly used as optimization criteria for quantum chemical high throughput calculations[30].

Methods

Materials: ZnO-N10 was purchased from Avantama AG. $PC_{70}BM$ was purchased from Solenne. ITIC was purchased from 1-Material. o-IDTBR was purchased from Flexink. eh-IDTBR was purchased from 1-Material. Y6 was purchased from Derthon OPV. WF3, WF3S, WF3F, WF3FS were synthesized in-house at Advent Technologies Inc.

Fabrication of Photovoltaic Devices: Pre-structured indium tin oxide substrates were cleaned with detergent followed by two 20 min ultrasonification steps in acetone and isopropanol. Subsequently a 10 min UV-ozone treatment was applied. A 30 nm thick layer of ZnO was doctor bladed in air and annealed at 200°C for 5 min after which the samples were moved into the glovebox. The active layer was spin-coated (30 s) from a solution which was kept at 120 °C and the rotation speed was adjusted to yield an active layer thicknesses of 120 nm. Immediately after spin coating an annealing step at 120 °C for 5 min was applied. 1,2-Dichlorobenzene was used as the solvent and the polymer:acceptor ratio and total concentration

was for 1:1.5 and 20 mg/mL for polymer:$PC_{70}BM$, 1:1.1 and 15 mg/mL for polymer:ITIC, 1:1.2 and 16 mg/mL for polymer:Y6, 1:1.1 and 15 mg/mL for polymer:eh-IDTBR, 1:1.1 and 15 mg/mL for polymer:o-IDTBR. To complete device fabrication 12 nm of MoO_3 and 100 nm of Ag were thermally evaporated through a mask (opening for active area was 10.4 mm^2) in a vacuum of ~10^{-6} mbar.

J-V measurement: The *J-V* characteristics were measured using a source measurement unit Keysight B2901A. Illumination was provided by a solar simulator (Oriel Sol 1A, from Newport) with AM1.5 G spectrum at 100 $mWcm^{-2}$.

EQE characterization: External quantum efficiency measurements were conducted using an integrated system from Enlitech (QE-R).

IQE calculations: Internal quantum efficiency calculations were performed based on the measured EQE and reflection of devices and on the parasitic absorption which was calculated based on a full optical transfer-matrix model, as described by Burkhard and coworkers[31]. EQE measurements of devices were performed as described above. Reflection measurements of devices were recorded with the integrating sphere of a commercial UV-vis spectrometer by Perkin Elmer (Lambda 950). Refractive indices of electrodes and interlayers were taken from https://refractiveindex.info, while the absorption coefficient of the active layer was measured with the integrating sphere of a UV-vis spectrometer by Perkin Elmer (Lambda 950). The active layer extinction coefficient is derived from the absorption coefficient, while we set n = 2 for the active layer. As described by Burkhard et al., setting n = 2 for the active layer will not significantly affect the calculated IQE for devices which exhibit high values of EQE, as is the case for our solar cells.

FTPS measurements: Fourier-transform photocurrent spectroscopy was carried out using a modified Vertex 70 FTIR spectrometer from Brucker optics GmbH with the solar cell acting as

the external detector. A low noise current amplifier (Femto, DLPCA-200) was used to amplify the photocurrent. Long pass cut-off filters were used to increase the signal to noise ratio further, allowing for highly precise measurements.

EL: Electroluminescence measurements were performed by applying a forward voltage to the solar cell and thereby operating the device as an LED. The emitted light was dispersed by an iHR-320 monochromator (Horiba) and detected by a liquid nitrogen cooled InGaAs detector.

Steady-state PL: Photoluminescence measurements were performed by using the 488 nm line of an argon-ion laser for excitation. The emitted light was dispersed by an iHR-320 monochromator (Horiba) and detected by a Peltier-cooled silicon CCD detector or a liquid nitrogen cooled InGaAs detector.

Time-resolved PL: Time-resolved photoluminescence measurements were performed by using the commercial setup Fluotime 300 from Picoquant. The setup was operated in the Time-Correlated Single Photon Counting (TCSPC) mode. Pulsed laser diodes were used for excitation and the wavelength was 402 nm (for $PC_{70}BM$, ITIC, eh-IDTBR and o-IDTBR based systems) or 783 nm (for Y6 based systems). For the 402 nm laser diode the FWHM was 150 ps and for the 783 nm laser diode it was 300 ps. The time-resolved PL emission was detected with a single photon counting PMT detector. Fits of the experimental data were performed by using the internal software.

Cyclic voltammetry: Cyclic voltammetry measurements were performed to detect the HOMO levels of films. The thin films were deposited directly on glass/ITO, which serves as the working electrode. The counter electrode was a coiled platinum wire and the reference electrode was Ag/AgCl. Ferrocene was used to double-check the Ag/AgCl reference electrode. A 0.05 M tetrabutylammonium hexafluorophosphate (TBAHFP) anhydrous acetonitrile solution was used as electrolyte. Prior to each measurement, the electrolyte was thoroughly degassed by N_2

bubbling for 20 min. The scan rate was 20 mV/s. The measurements were performed by using the Electro-chemical workstation ZENNIUM Pro by Zahner-Elektrik, and the data was recorded with the internal cyclic voltammetry software.

Theoretical calculations: All calculations of the model compounds studied in this work have been performed using the Gaussian 09 software package. The alkyl side chains substituents anchored onto the benzodithiophene and quinoxaline have been replaced with methyl groups in the model compounds for our calculations. While the presence of these long alkyl chains enhances the solubility of these polymers and affects the charge carrier mobility and photovoltaic behavior of the polymer,[32–34] from a computational point of view their replacement with shorter chains does not affect their optoelectronic properties (E_{HOMO}, E_{LUMO} and band gap) and thus the optimized structures of the molecules.[35,36] The ground state geometry of each model compound has been determined by a full geometry optimization of its structural parameters using the DFT calculations, upon energy minimization of all possible isomers. In this work, the DFT calculations were performed using the HSEH1PBE/6-311G(d,p) basis set. All calculations were performed taking into account that the system is under vacuum conditions. No symmetry constraints were imposed during the optimization process. The geometry optimizations have been performed with a tight threshold that corresponds to root mean square (rms) residual forces smaller than 10^{-5} au for the optimal geometry. The energy level of the E_{HOMO} and the E_{LUMO} of the repetitive units of each polymer were carried out by using the same set of calculations. DFT/HSEH1PBE/6-311G has been found[37] to be an accurate formalism for calculating the structural and electronic properties of many molecular systems. In our studies the theoretical calculations performed on dimer model compounds. The visualization of the molecular orbitals has been performed using GaussView 5,0.

Voltage loss calculation: The band gap to V_{OC} loss and the non-radiative voltage loss ($\Delta V_{OC,non\text{-}rad}$) were calculated by determining the band gap from accurate EQE measurements and by determining the radiative V_{OC} ($V_{OC,rad}$) of all solar cells. The radiative V_{OC} describes the thermodynamic voltage limit of a solar cell in the absence of non-radiative charge carrier recombination and it is calculated by

$$V_{OC,rad} = \frac{k_B T}{q} \cdot \ln\left(\frac{J_{SC}}{J_{0,rad}} + 1\right),$$

with J_{SC} being the short circuit current at AM1.5 G illumination and $J_{0,rad}$ being the dark saturation current for a solar cell in thermal equilibrium at room temperature, in the radiative limit. Here, $J_{0,rad}$ is derived from the EQE(E) via,

$$J_{0,rad} = q \cdot \int_0^\infty EQE(E) \cdot \Phi_{BB,300K}(E)\ dE.$$

With q being the elementary charge and $\Phi_{BB,300K}(E) = \frac{2\pi E^2}{h^3 c^2} \exp\left(-\frac{E}{k_B T}\right)$ being the black body spectrum of a semiconductor at room temperature. According the latter equation one has to integrate over the whole energy range from zero energy to infinitely high energies and as even very precise EQE measurements may exhibit too much noise, the detailed balance relation is utilized to combine EL with FTPS measurements to calculate $J_{0,rad}$. Knowledge of $V_{OC,rad}$, allows to directly calculate non-radiative voltage losses by using

$$\Delta V_{OC,non-rad} = V_{OC,rad} - V_{OC}.$$

Utilizing EQE, EL and the upper 3 equations, the band gap to V_{OC} loss as well as $\Delta V_{OC,non\text{-}rad}$ for all investigated systems were determined.

Data availability

All data generated or analyzed during this study are included in the published article and its Supplementary Information and Source Data files.

Conflict of Interest

The authors declare no conflict of interest.

Acknowledgements

A.C. and C.J.B. gratefully acknowledge funding by the Deutsche Forschungsgemeinschaft (DFG, German Research Foundation) – Projektnummer 182849149 – SFB 953. C.J.B. gratefully acknowledges the financial support through the "Aufbruch Bayern" initiative of the state of Bavaria (EnCN and SFF) and the Bavarian Initiative "Solar Technologies go Hybrid" (SolTech) and funding from DFG project DFG INST 90/917. C. C. L would like to thank the European Union for the financial support. This project has received funding from the European Union's Horizon 2020 research and innovation programme under grant agreements No 761112 (PRESTIGE) and No 820789 (OLEDSOLAR).

Author contributions

T.H. and C.J.B. conceived the idea for this study and supervised this work. A.C. fabricated all measured devices and samples, performed JV-characterization, EQE measurements, FPTS spectroscopy, CV measurements and absorbance measurements. C.L.C and V.G.G. synthesized the polymers used in this work and performed DFT calculations. A.O. and A.C. performed TRPL measurements. J.W. and A.C. performed steady-state PL and EL measurements. K.F. performed optical transfer-matrix calculation of IQE. L.L. developed the effective two-states model and utilized this theoretical framework to fit the experimental data. T.H., I.M., C.J.B. and A.C. evaluated and interpreted the experimental findings. The manuscript was written and commented on by all authors.

References

1. Green, M. A. *et al.* Solar cell efficiency tables (Version 53). *Prog. Photovoltaics* **2**, 3–12 (2019).
2. Xu, X. *et al.* Single-Junction Polymer Solar Cells with 16.35% Efficiency Enabled by a Platinum(II) Complexation Strategy. *Adv. Mater.* **1901872**, 1901872 (2019).
3. Liu, Z. *et al.* Open-Circuit Voltages Exceeding 1.26 V in Planar Methylammonium Lead Iodide Perovskite Solar Cells - SUP. *ACS Energy Lett.* **1**, 110–117 (2018).
4. Polman, A., Knight, M., Garnett, E. C., Ehrler, B. & Sinke, W. C. Photovoltaic materials: Present efficiencies and future challenges. *Science (80-.).* **352**, (2016).
5. Geisz, J. F., Steiner, M. A., García, I., Kurtz, S. R. & Friedman, D. J. Enhanced external radiative efficiency for 20.8% efficient single-junction GaInP solar cells. *Appl. Phys. Lett.* **103**, 0–5 (2013).
6. Miller, O. D., Yablonovitch, E. & Kurtz, S. R. Intense internal and external fluorescence as solar cell approach the SQ efficiency limit. *Photovoltaics, IEEE J.* **2**, 1–27 (2012).
7. Deibel, C. & Dyakonov, V. Polymer–fullerene bulk heterojunction solar cells. *Reports Prog. Phys.* **73**, 96401 (2010).
8. Green, M. A. *et al.* Solar cell efficiency tables (version 50). *Prog. Photovoltaics Res. Appl.* **25**, 668–676 (2017).
9. Zheng, Z. *et al.* Efficient Charge Transfer and Fine-Tuned Energy Level Alignment in a THF-Processed Fullerene-Free Organic Solar Cell with 11.3% Efficiency - SUP. *Adv. Mater.* **29**, (2017).
10. Qian, D. *et al.* Design rules for minimizing voltage losses in high-efficiency organic solar cells. *Nat. Mater.* **17**, 703–709 (2018).

11. Eisner, F. *et al.* Hybridization of Local Exciton and Charge-Transfer States Reduces Non-Radiative Voltage Losses in Organic Solar Cells. *J. Am. Chem. Soc.* jacs.9b01465 (2019) doi:10.1021/jacs.9b01465.

12. Holliday, S. *et al.* High-efficiency and air-stable P3HT-based polymer solar cells with a new non-fullerene acceptor - SUP. *Nat. Commun.* (2016).

13. Lin, Y. *et al.* An Electron Acceptor Challenging Fullerenes for Effi cient Polymer Solar Cells. *Adv. Mater.* **27**, 1170–1174 (2015).

14. Yuan, J. *et al.* Single-Junction Organic Solar Cell with over 15 % Efficiency Using Fused-Ring Acceptor with Electron-Deficient Core. *Joule* **3**, 1–12 (2019).

15. Fan, B. *et al.* Achieving over 16% efficiency for single-junction organic solar cells. *Sci. China Chem.* (2019) doi:10.1007/s11426-019-9457-5.

16. Sweetnam, S. *et al.* Characterization of the polymer energy landscape in polymer:fullerene bulk heterojunctions with pure and mixed phases. *J. Am. Chem. Soc.* **136**, 14078–14088 (2014).

17. Dong, Y. *et al.* The binding energy and dynamics of charge-transfer states in organic photovoltaics with low driving force for charge separation. *J. Chem. Phys.* **150**, (2019).

18. Xie, Y. *et al.* Assessing the energy offset at the electron donor/acceptor interface in organic solar cells through radiative efficiency measurements. *Energy Environ. Sci.* **12**, 3556–3566 (2019).

19. Falke, S. M. *et al.* Coherent ultrafast charge transfer in an organic photovoltaic blend. *Science (80-.).* **344**, 1001–1005 (2014).

20. Howard, I. A., Mauer, R., Meister, M. & Laquai, F. Effect of morphology on ultrafast free carrier generation in polythiophene:fullerene organic solar cells. *J. Am. Chem. Soc.* **132**, 14866–14876 (2010).

21. Ziffer, M. E. *et al.* Long-Lived, Non-Geminate, Radiative Recombination of Photogenerated Charges in a Polymer/Small-Molecule Acceptor Photovoltaic Blend. *J. Am. Chem. Soc.* **140**, 9996–10008 (2018).

22. Gélinas, S., Poll, T. S. Van Der, Bazan, G. C. & Friend, R. H. Ultrafast Long-Range Charge Seperation in Organic Semiconductor Photovoltaic Diodes. **512**, 512–517 (2014).

23. Vandewal, K., Benduhn, J. & Nikolis, V. C. How to determine optical gaps and voltage losses in organic photovoltaic materials. *Sustain. Energy Fuels* **2**, 538–544 (2018).

24. Rau, U., Blank, B., Müller, T. C. M. & Kirchartz, T. Efficiency Potential of Photovoltaic Materials and Devices Unveiled by Detailed-Balance Analysis. *Phys. Rev. Appl.* **7**, 1–9 (2017).

25. Classen, A. *et al.* Absence of Charge Transfer State Enables Very Low V OC Losses in SWCNT:Fullerene Solar Cells. *Adv. Energy Mater.* **9**, 1801913 (2018).

26. Kirchartz, T. & Rau, U. Detailed balance and reciprocity in solar cells. *Phys. Status Solidi Appl. Mater. Sci.* **205**, 2737–2751 (2008).

27. Rau, U. Reciprocity relation between photovoltaic quantum efficiency and electroluminescent emission of solar cells. *Phys. Rev. B - Condens. Matter Mater. Phys.* **76**, 1–8 (2007).

28. Benduhn, J. *et al.* Intrinsic non-radiative voltage losses in fullerene-based organic solar cells - SUP. *Nat. Energy* **2**, 17053 (2017).

29. Heiber, M. C., Baumbach, C., Dyakonov, V. & Deibel, C. Encounter-limited charge-carrier recombination in phase-separated organic semiconductor blends. *Phys. Rev. Lett.* **114**, 1–5 (2015).

30. Lopez, S. A., Sanchez-Lengeling, B., de Goes Soares, J. & Aspuru-Guzik, A. Design Principles and Top Non-Fullerene Acceptor Candidates for Organic Photovoltaics. *Joule* **1**,

857–870 (2017).

31. Burkhard, G. F., Hoke, E. T. & McGehee, M. D. Accounting for interference, scattering, and electrode absorption to make accurate internal quantum efficiency measurements in organic and other thin solar cells. *Adv. Mater.* **22**, 3293–3297 (2010).

32. Bronstein, H. *et al.* Indacenodithiophene-co-benzothiadiazole copolymers for high performance solar cells or transistors via alkyl chain optimization. *Macromolecules* **44**, 6649–6652 (2011).

33. Biniek, L. *et al.* Optimization of the side-chain density to improve the charge transport and photovoltaic performances of a low band gap copolymer. *Org. Electron.* **13**, 114–120 (2012).

34. Biniek, L. *et al.* 3,6-Dialkylthieno[3,2-b]thiophene moiety as a soluble and electron donating unit preserving the coplanarity of photovoltaic low band gap copolymers. *J. Polym. Sci. Part A Polym. Chem.* **50**, 1861–1868 (2012).

35. Risko, C., McGehee, M. D. & Brédas, J. L. A quantum-chemical perspective into low optical-gap polymers for highly-efficient organic solar cells. *Chem. Sci.* **2**, 1200–1218 (2011).

36. Ku, J., Lansac, Y. & Jang, Y. H. Time-dependent density functional theory study on benzothiadiazole-based low-band-gap fused-ring copolymers for organic solar cell applications. *J. Phys. Chem. C* **115**, 21508–21516 (2011).

37. Chochos, C. L. *et al.* Experimental and theoretical investigations on the optical and electrochemical properties of π-conjugated donor-acceptor-donor (DAD) compounds toward a universal model. *J. Chem. Phys.* **149**, (2018).